PAPER

Check for updates

Electronic structure modulation of MOF-based host–guest recognition polymer electrolytes for high-performance all-solid-state sodium metal batteries

Xiaorong Dong,[a,b] Huan Chen,[a,b] B. V. R. Chowdari,[c] Xiangwei Wu*[a,b] and Zhaoyin Wen [ID] *[a,b]

Transitioning from gel to all-solid-state sodium metal batteries (ASSMBs) is essential for upgrading the energy density and safety of flexible energy storage devices. Herein, a novel host–guest recognition strategy for all-solid-state composite polymer electrolytes (CPEs) is proposed by introducing an Fe–Ni bimetallic metal–organic framework (MOF) into the PEO matrix. The Fe–Ni MOF with various synergetic sites serves as a 'host' platform for CPEs to weaken the coulombic interaction between Na$^+$ and bis(trifluoromethysulfonyl)imide (TFSI$^-$), thereby promoting the dissociation of sodium salt. They reduce the Na$^+$ migration barrier and improve high-voltage stability. The optimized CPE achieves an ionic conductivity of 1.37×10^{-4} S cm^{-1} at 30 °C, and the Na$^+$ transference number increased threefold (from 0.23 to 0.63). The corresponding Na//Na symmetric cells operate stably for 1150 h at 25 °C, and the Na//Na$_3$V$_2$(PO$_4$)$_3$ (NVP) cells demonstrate 97.2% capacity retention after 600 cycles at 1C. Thanks to the high oxidation limit of the CPE (4.5 V), the Na$_3$V$_2$(PO$_4$)$_2$F$_3$ (NVPF)-based ASSMBs demonstrate stable cycling over 500 cycles within the voltage range of 2.5–4.3 V. Furthermore, an all-solid-state Na metal pouch cell exhibits a high initial discharge specific capacity of 113.4 mAh g^{-1} and remains stable for 56 cycles at 0.1C. This innovative host–guest recognition polymer electrolyte offers valuable insights for enhancing rapid ion transport and contributing to the better understanding of the underlying Na$^+$ kinetics mechanisms.

Broader context

Solid polymer electrolyte (SPE)-based sodium metal batteries (SMBs) are promising next-generation lightweight energy storage materials, combining excellent processability with cost-effectiveness. Transitioning from gel-state to all-solid-state sodium metal batteries (ASSMBs) is a necessary step to enhance both safety and energy density. However, the removal of solvents or unpolymerized monomers in SPEs often results in intrinsically low ionic conductivity (below 10^{-5} S cm^{-1} at room temperature), low Na$^+$ transference numbers ($t_{Na^+} < 0.3$), and poor interfacial compatibility with electrodes. Herein, a host–guest recognition strategy was designed for polymer electrolytes by incorporating bimetallic metal–organic frameworks (MOFs) with abundant Lewis acid sites into the polymer matrix. Tailoring the electronic configuration of the bimetallic MOFs enables them to effectively capture TFSI$^-$ anions and accelerate the dissociation–desorption of Na$^+$ along the PEO chains. The unique system achieves an ionic conductivity of 1.37×10^{-4} S cm^{-1} at 30 °C, which ranks among the highest reported for all-solid-state polymer systems to date, and a t_{Na^+} of 0.63, along with a wide electrochemical oxidation window. Specifically, the NVP//Na ASSMB demonstrates a high reversible capacity of 100.6 mAh g^{-1} and good cycling stability with 97.2% capacity retention after 600 cycles at 1C. Furthermore, the all-solid-state sodium metal pouch cells achieved an impressive initial discharge specific capacity of 113.4 mAh g^{-1} and remained stable for 56 cycles at 0.1C. This work proposes a promising host–guest recognition strategy for SPEs to enhance Na$^+$ transport, providing valuable insights for the design of next-generation all-solid-state electrolyte systems with high energy density.

[a] The State Key Lab High Performance Ceram & Superfine Microstructure, Shanghai Institute of Ceramics Chinese Academy of Sciences, Shanghai 200050, P. R. China. E-mail: xwwu@mail.sic.ac.cn, zywen@mail.sic.ac.cn
[b] Center of Materials Science and Optoelectronics Engineering, University of Chinese Academy of Sciences, Beijing 100049, P. R. China
[c] School of Materials Science and Engineering, Nanyang Technological University, 639798, Singapore

Introduction

Sodium metal has a high theoretical specific capacity (1165 mAh g^{-1}) and a low redox potential (−2.714 V *vs.* the standard hydrogen electrode),[1] making sodium metal batteries (SMBs) an important form of high-energy-density energy storage systems.[2,3] Traditional SMBs use organic liquid electrolytes, where the organic solvents are highly flammable, prone

to leakage, and susceptible to severe side reactions with the chemically reactive Na metal.[4] Therefore, the large-scale application of SMBs still faces significant challenges. Consequently, substituting traditional liquid electrolytes with solid-state electrolytes (SSEs) has been proven to be a viable strategy.[5] Among various SSEs, solid polymer electrolytes (SPEs) have significant advantages in improving battery safety, enhancing mechanical properties, preventing uncontrolled dendrite formation, and exhibiting high electrochemical stability.[6] Polyethylene oxide (PEO)-based SPEs have been extensively studied owing to their excellent salt solubility.[7] The ether oxygen groups on PEO exhibit strong coordination interactions with Na^+, which is beneficial for the dissolution of sodium salts. However, these strong interactions hinder the migration of Na^+, resulting in a low Na^+ transference number (t^+) leading to severe concentration polarization and thus uneven sodium deposition and ultimately dendrite formation.[8,9] Therefore, achieving a balance between high ionic conductivity and t^+ while maintaining stable electrochemical performance is a key challenge for all-solid-state sodium metal batteries (ASSMBs) based on SPEs.

In recent years, development of single sodium ion conductive SPEs by bonding anions to the main chain of polymers to suppress anion migration has significantly improved the Na^+ transference number.[10] However, the ionic conductivity remains relatively low, making battery operation difficult. Incorporating fillers into the polymer matrix has been shown to be a promising approach to enhance the ionic conductivity of SPEs.[11] Metal–organic frameworks (MOFs) have advantages including large pore volume, high surface area, adjustable pore size, and diverse topological structures. They provide a new method for the design of composite polymer electrolytes (CPEs).[12] The excellent specific surface area of MOFs provides closely packed cation hopping sites reducing the activation energy required for ion transfer and increasing ionic conductivity.[13] The ordered porosity of MOFs can also regulate the uniform deposition of Na^+ on the anode and suppress dendrite formation.[14] Additionally, the strong coordination interaction between the unsaturated metal sites exposed in MOFs after removing solvent molecules and the anions in sodium salts can balance the charge and maximize the Na^+ transference number.[15] Meanwhile, incorporating MOFs into polymer electrolytes can effectively reduce polymer crystallinity, increase the amorphous fraction, and promote Na^+ transport through anion capture and continuous migration channels.[16–19] The utilization of MOFs as fillers in SPEs has significantly influenced the development of CPEs, leading to improved electrochemical performance.[20] However, the critical role of MOFs in CPEs and their Na^+ migration mechanisms are not fully understood.[21] Therefore, further research is necessary to improve our understanding of the critical role of MOFs in SMBs.[22]

In this work, we propose a novel host–guest recognition MOF-CPE strategy for SMBs. A bimetallic Fe–Ni MOF with anion-trapping effects was introduced into a PEO-based electrolyte for developing a composite polymer electrolyte with the addition of 10% Fe–Ni MOF (CPE-10) to selectively enhance Na^+ migration capability and achieve ultra-stable ASSMBs. In CPE-10, the abundant Lewis-acid sites exposed on the bimetallic Fe–Ni MOF can inhibit the migration of $TFSI^-$ through strong anion-trapping effects. This unique structure, combined with the synergistic effect of highly promoted sodium salt dissociation, provides a long-range, efficient, and continuous pathway for selective and rapid Na^+ transport. This significantly enhances the ionic conductivity (1.37×10^{-4} S cm^{-1}, 30 °C) and the Na^+ transference number (0.63) of the CPE. Molecular dynamics (MD) simulations elucidate that the Fe–Ni MOF has strong anion-trapping effects, endowing CPE-10 with robust Na^+ transport capability and coordination environments. The Na/Na cell demonstrates stable cycling for 1150 h at 25 °C. Furthermore, the $Na_3V_2(PO_4)_3$ (NVP)/CPE-10/Na cell exhibits excellent cycling stability and rate performance at 25 °C and 60 °C. Moreover, the pouch cell delivers an initial discharge specific capacity close to its theoretical capacity and maintains stable cycling at a high loading of nearly 4 mg cm^{-2}. This work lays the foundation for long lifespan and large-scale ASSMBs.

Results and discussion

Design rationale of the Fe–Ni MOF structure

In conventional PEO-based solid polymer electrolytes, strong $O–Na^+$ coordination significantly impedes Na^+ migration, resulting in a low t^+. To address this issue, the Fe–Ni bimetallic MOF is introduced as a functional filler to weaken $O–Na^+$ coordination, thereby significantly accelerating the dissociation of Na salts. Following dissociation, it is essential to inhibit the complexation of Na^+ with $TFSI^-$ to increase the availability of active Na^+ (Fig. 1a). To fulfill the requirements for efficient "host" functionality, theoretical calculations were employed to screen nine representative metal MOF materials for their adsorption energy of $TFSI^-$ in sodium salts. This analysis covers the adsorption energies of five monometallic MOFs and four bimetallic MOFs, with ligands of trimesic acid. As depicted in Fig. 1b, the Fe–Ni bimetallic MOF exhibits the highest adsorption energy for $TFSI^-$, while the monometallic Fe MOF and Ni MOF show the lowest adsorption energies. In the Fe–Ni MOF structure, the projected density of states (PDOS) reveals that the d states of the Fe center are closer to the Fermi level (E) than those of the Ni center (Fig. 1c). This indicates that the d-orbitals of Fe are the main active orbitals, determining the adsorption strength of Na and the catalytic activity of the Fe–Ni MOF. It also demonstrates that the introduction of Fe into the monometallic MOF(Ni) results in more electronic states within a specific energy range, enhancing the opportunities for electron exchange with reactants. Therefore, the Fe–Ni bimetallic MOF was ultimately chosen as the filler for the PEO matrix for the following reasons: (1) in the Fe–Ni bimetallic MOF, the d-band center of the Fe sites is closer to the Fermi level compared to single-metal MOFs, which significantly enhances the adsorption ability for F/O in $TFSI^-$.
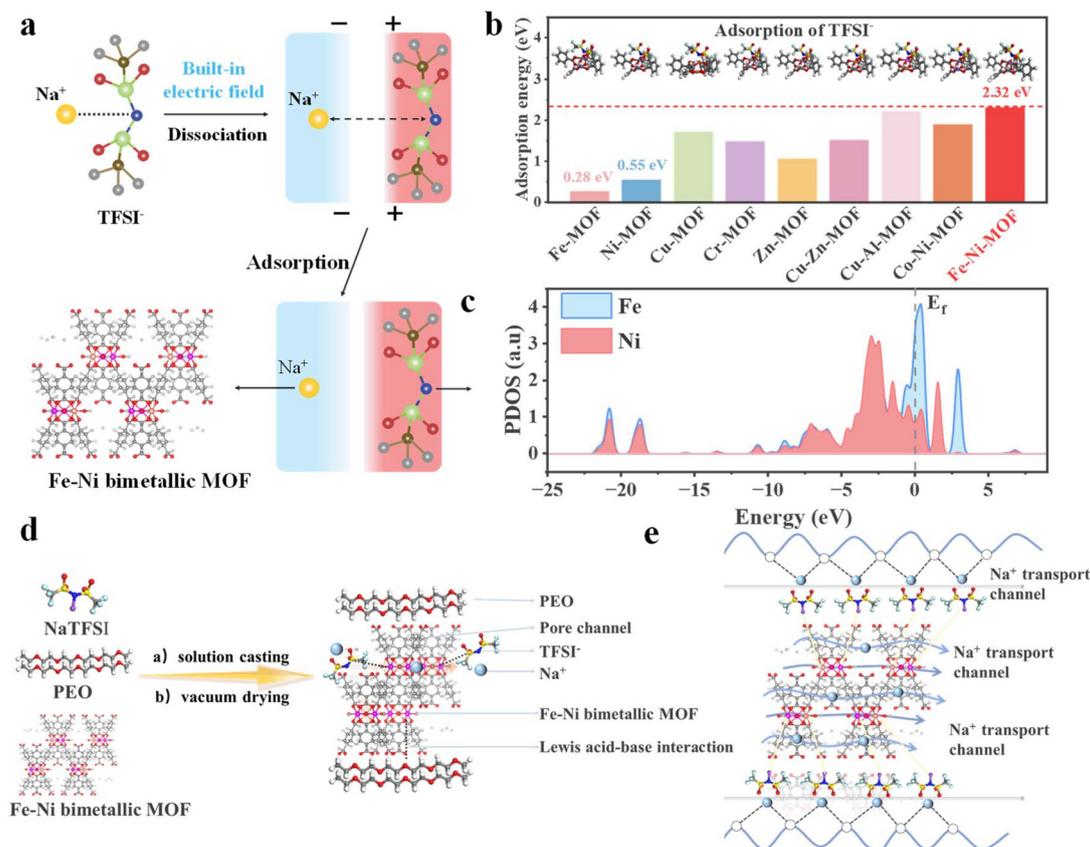
Fig. 1 (a) Detailed depiction of the dissociation and adsorption mechanisms of NaTFSI. (b) Theoretical calculations that screen the adsorption energy of TFSI⁻ on reported and representative single-metal and bimetallic MOFs. (c) DFT-calculated DOS of MOF(Fe–Ni). (d) Schematic diagram of CPE synthesis. (e) Schematic illustration of the Fe–Ni MOF-enhanced structure of CPEs with selective and rapid Na⁺ transport.

Besides, the d-band center of the Ni sites shifts upward, avoiding the issue of difficult anion desorption seen in the single Ni-MOF due to a deeper d-band center. This synergistic electronic structure allows for "moderate anion adsorption", meeting the ion adsorption–desorption balance required for electrolyte fillers.[23] (2) The unique Fe–O–Ni–O–Fe bonding pathway creates an efficient electron transfer channel. The Ni sites act as electron donors, continuously supplying electrons to the Fe sites through the d–π conjugation effect.[24] This charge distribution mechanism is not achievable in single-metal MOFs. It enhances the Fe sites' adsorption capacity and prevents the Ni sites from excessive electron localization, which could lead to strong adsorption and poisoning of active sites. (3) The electron delocalization effect in the Fe–Ni bimetallic MOF effectively disperses the negative charge of TFSI⁻, reducing steric hindrance, while maintaining high ionic conductivity and ensuring strong adsorption.[25] To sum up, the synergistic effect of Fe and Ni sites in the Fe–Ni bimetallic MOF addresses the issues of anion adsorption–desorption balance found in single-metal MOFs, making it the optimal choice.

The introduction of the Fe–Ni MOF into the PEO-based electrolyte creates a homogeneous structure, providing a continuous linear path for rapid ion transport, thus reducing the activation energy required for Na⁺ migration, referred to as CPE-10 (Fig. 1d). Additionally, the increase in amorphous regions within the PEO matrix in CPE-10, induced by the interaction between the numerous metal sites in the MOF and the ether oxygen bonds in PEO, leads to the opening of polymer chains. This improves ionic conductivity and synergistically facilitates rapid Na⁺ transport within the system. On the other hand, the numerous metal sites in the Fe–Ni MOF act as Lewis-acid sites which can constrain TFSI⁻ to accelerate sodium salt dissociation and balance charges while increasing the free state of Na⁺ that can participate in complexation. This results in the increase of the Na⁺ transference number and reduces concentration polarization and ohmic polarization within CPE-10 due to uneven ion distribution.[26] Consequently, CPE-10 is expected to achieve both high ionic conductivity and a high Na⁺ transference number, therefore enabling ultralong cycling life in ASSMBs (Fig. 1e).

Design and characterization of the host–guest recognition electrolyte

Scanning electron microscopy (SEM) and transmission electron microscopy (TEM) were used to observe the morphology

Paper

of the Fe–Ni MOF. As shown in Fig. 2a (SEM) and 2b (TEM), the Fe–Ni MOF is composed of uniformly stacked three-dimensional cauliflower shaped structures arranged in a lamellar stack. This uniform and well-ordered nanostructure facilitates sufficient contact between the electrolyte and the MOF, thereby providing more effective migration pathways for Na$^+$ and enhancing ionic conductivity. Energy dispersive X-ray spectroscopy (EDS) results confirmed the uniform distribution of Fe, Ni, C, and O elements on the surface of the Fe–Ni MOF (Fig. S1). The uniform distribution of elements ensures that the Lewis acid sites are evenly distributed across the MOF surface, which helps to uniformly capture TFSI$^-$ anions and optimize Na$^+$ migration pathways and the transference number. The Fe–Ni MOF features high Lewis acidity, which makes it a promising solid catalyst.[27] Therefore, these Fe–Ni MOF nanocrystals enable the exposure of more active sites,

leading to a more sufficient interaction with C–O–C segments, which are considered as Lewis-base centers in PEO chains.[28] Brunauer–Emmett–Teller (BET) results indicated that the Fe–Ni MOF has a large specific surface area (284.0 m^2 g^{-1}) (Fig. S2a).[29] The microporous structure of the Fe–Ni MOF can selectively restrict the passage of TFSI$^-$, thus enhancing the Na$^+$ transference number (Fig. S2b).[30] The larger specific surface area provides more accessible active surfaces and microporous spaces, offering additional migration pathways for Na$^+$ and thereby enhancing the ionic conductivity of the electrolyte. To highlight the advantages of the Fe–Ni bimetallic MOF, we synthesized an Fe-MOF and a Ni-MOF using the same experimental methods and tested their specific surface areas and porosity (Fig. S3). The results showed that the specific surface area of the Fe–Ni bimetallic MOF is more than three times that of the Fe-MOF and 28 times that of the Ni-MOF.
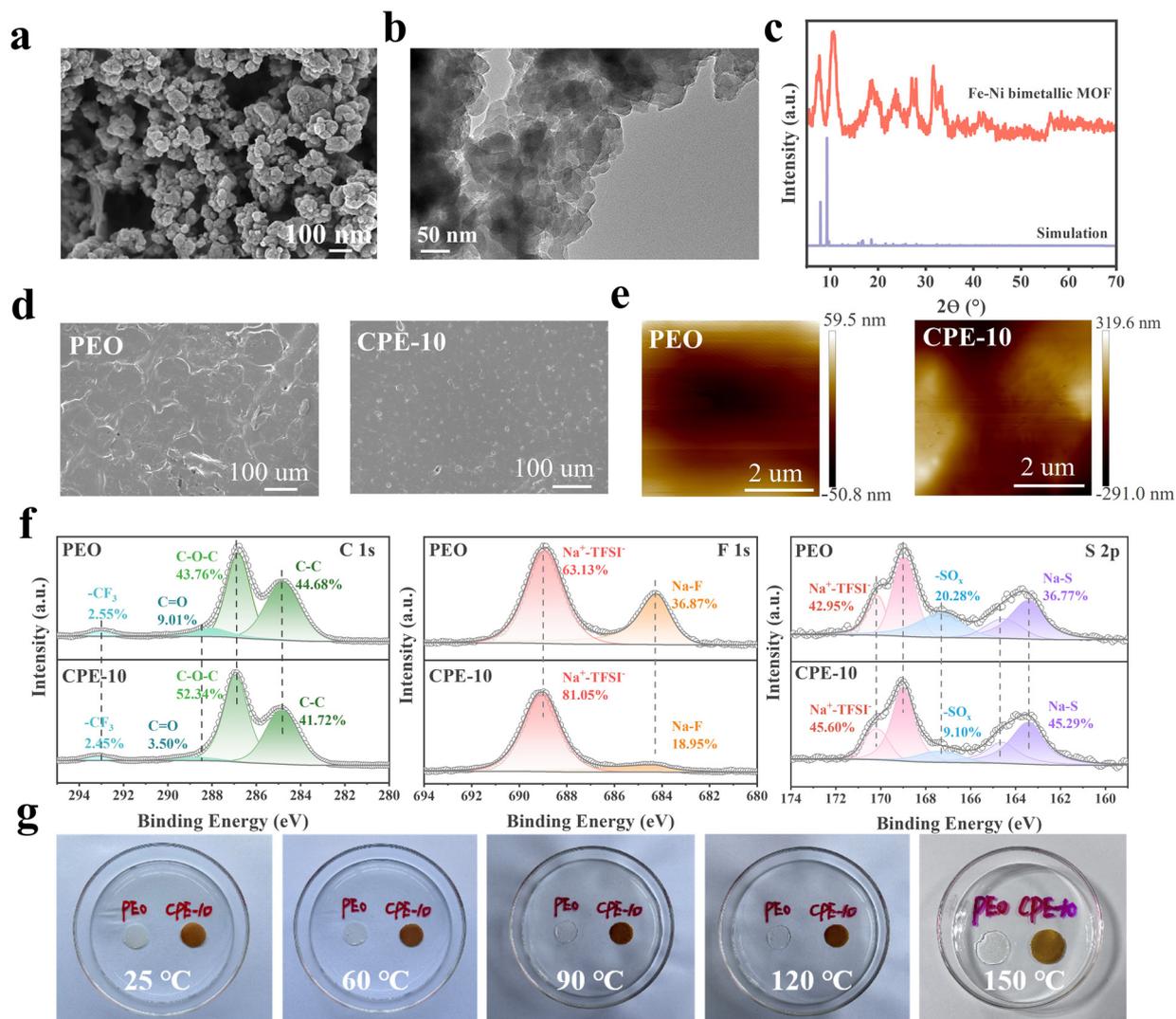
Fig. 2 (a) SEM image and (b) TEM image of the as-prepared Fe–Ni MOF powder. (c) XRD and simulated XRD patterns of the Fe–Ni MOF. (d) SEM images of PEO and CPE-10. (e) Surface morphologies of PEO and CPE-10 obtained by AFM. High-resolution XPS spectra of (f) C 1s, (g) F 1s and (h) S 2p for PEO and CPE-10 membranes. (g) Optical photographs of the states of PEO and CPE-10 membranes at 25, 60, 90, 120 and 150 °C.

This indicates that the design of the bimetallic MOF optimizes its structure, significantly increasing the specific surface area and the number of exposed Lewis-acid sites. This enhancement is beneficial for optimizing the host functions of the bimetallic MOF and strengthening its effective recognition of guest molecules. While all metal MOFs can ensure the presence of Na^+ within their microporous structures, the bimetallic MOF system releases more dissociated Na^+, effectively facilitating the rapid migration and diffusion of Na^+. Furthermore, the X-ray diffraction (XRD) spectrum of the Fe–Ni MOF exhibited peaks at positions consistent with the standard Fe–Ni MOF XRD pattern, with characteristic diffraction peaks at 7.7° and 10.6° (Fig. 2c). However, both peaks exhibited a slight low-angle shift, possibly due to the nanoscaling and defect doping of the Fe–Ni MOF.[27] The crystallinity of the Fe–Ni MOF was also enhanced, attributed to the loss of organic components during the hydrothermal process. This results in slight growth of the three-dimensional cauliflower shaped structures of the Fe–Ni MOF and exposes more effective Lewis-acid sites on the surface of the nanosheet material, thus facilitating better interaction with the PEO-based electrolyte components.[31] X-ray photoelectron spectroscopy (XPS) was used to determine the surface composition and chemical states of elements in the Fe–Ni MOF. The C 1s spectrum was fitted with three peaks centered at 284.8 eV, 286.3 eV and 288.4 eV, corresponding to C–C, C–O, and C=O bonds, respectively.[32] The O 1s spectrum revealed the presence of –OH peaks at 531.7 eV and C=O bonds at 532.8 eV. Furthermore, the Fe 2p XPS curve showed two chemically distinct substances, including metallic iron and oxidized iron states.[33] The Ni 2p spectrum showed peaks at 855.5 eV and 873.2 eV belonging to the oxidized state of Ni (Fig. S4).[34] The transition metals are successfully anchored onto the organic framework. The optical photograph of CPE-10 prepared by the solution casting method is shown in Fig. S5. The resulting brown film exhibits excellent flexibility, undergoing significant inelastic deformation when manually stretched. The stress–strain curve indicates that CPE-10 also possesses good mechanical strength and tensile performance (Fig. S6), with a Young's modulus as high as 35.0 MPa at room temperature, which helps to suppress the penetration of sodium dendrites. SEM analysis results show that the surface of CPE-10 is smoother and denser than that of PEO, which is beneficial for improving the interfacial contact between the electrolyte and the electrode (Fig. 2d). Such improved interface uniformity facilitates more efficient Na^+ transport across the electrode–electrolyte interface, and thus enhances the overall ionic conductivity and electrochemical performance of the cell. Atomic force microscopy (AFM) tests also revealed that the surface roughness did not change significantly after the introduction of inorganic fillers, indicating good dispersion and compatibility of the Fe–Ni MOF in the PEO matrix (Fig. 2e). This uniform dispersion helps Na^+ to migrate efficiently, improving ionic conductivity and electrochemical performance.

Fig. 2f presents the C 1s, F 1s, and S 2p XPS spectra of PEO and CPE-10 for comparative analysis. In the C 1s spectra of both electrolytes, four peaks were observed corresponding to C–C, C–O–C, C=O and –CF_3. The changes in peak area ratios indicate the interaction between PEO and the Fe–Ni MOF, leading to the disentanglement of polymer electrolyte chains in the PEO-based system. Furthermore, in the S 2p spectrum of CPE-10, the intensity of the –SO_x peak decreased, suggesting the suppression of $TFSI^-$ decomposition into –SO_x, which further demonstrates the high stability of the CPE-10 electrolyte. Additionally, in CPE-10, the Na–F peak area ratio decreased from 36.87% to 18.95%. Compared with PEO, more ion pairs (Na^+-$TFSI^-$) are formed after NaTFSI dissociation in the CPE-10 electrolyte. This is likely due to the strong electrostatic interaction between the Fe–Ni metallic MOF and $TFSI^-$, which facilitates the dissociation of NaTFSI and enhances the mobility of Na^+. CPE-10 maintains a stable shape with better mechanical properties even at high temperatures over 150 °C, highly improving the potential for safe application of PEO even if the temperature is over 90 °C (Fig. 2g).

Fig. 3a shows the thermogravimetric analysis (TGA) of CPE-10 and PEO. The addition of the Fe–Ni MOF increased the decomposition temperature of the electrolyte, effectively raising it from 200 °C to 304 °C. Due to the high thermal stability of the Fe–Ni MOF, the residual mass of the composite electrolyte remains as high as nearly 10% even at temperatures close to 600 °C. This residual proportion is consistent with Fe–Ni MOF content. XRD analysis results show that the Fe–Ni MOF did not alter the crystal structure of PEO (Fig. 3b). The peaks at 19° and 23° correspond to the crystalline regions of PEO, and their reduced intensity in CPE-10 indicates a decrease in crystallinity. The Fe–Ni MOF disrupts the regular packing of PEO chains through steric hindrance, weakening interchain van der Waals interactions and increasing the amorphous region, which provides more accessible Na^+ migration pathways. Additionally, the MOF's porous structure and Lewis acid sites interact with NaTFSI, capturing and dispersing anions and locally enriching Na^+, while also helping to form continuous migration channels that lower the Na^+ migration energy barrier. Together, these effects synergistically enhance the overall ionic conductivity of CPE-10.[35] Fig. S7 shows the DSC thermal curves of CPE-10 and PEO electrolytes in the temperature range of −60 to 100 °C, with the corresponding glass transition temperature (T_g), melting temperature (T_m), melting enthalpy (ΔH_m), and crystallinity (χ_c) listed in Table S1 (the method for calculating crystallinity can also be found in the SI). For CPE-10, the synchronous decrease of T_g, T_m, and ΔH_m (Table S1) indicates an expansion of the amorphous region. The XRD and DSC results demonstrate that the introduction of the Fe–Ni MOF with abundant unsaturated metal sites can disrupt the crystalline regions of the polymer, promote segmental chain motion, and thus inhibit the crystallization of the PEO matrix. To evaluate the effect of the Fe–Ni MOF developed on Na^+ migration in CPEs, the ionic conductivities at room temperature of various CPEs were measured (Fig. 3c and Fig. S8). It is found that CPE-10 exhibited the highest ionic conductivity, reaching 5.75×10^{-5} S cm^{-1}, almost an order of magnitude higher than that of PEO, Fe-MOF CPE
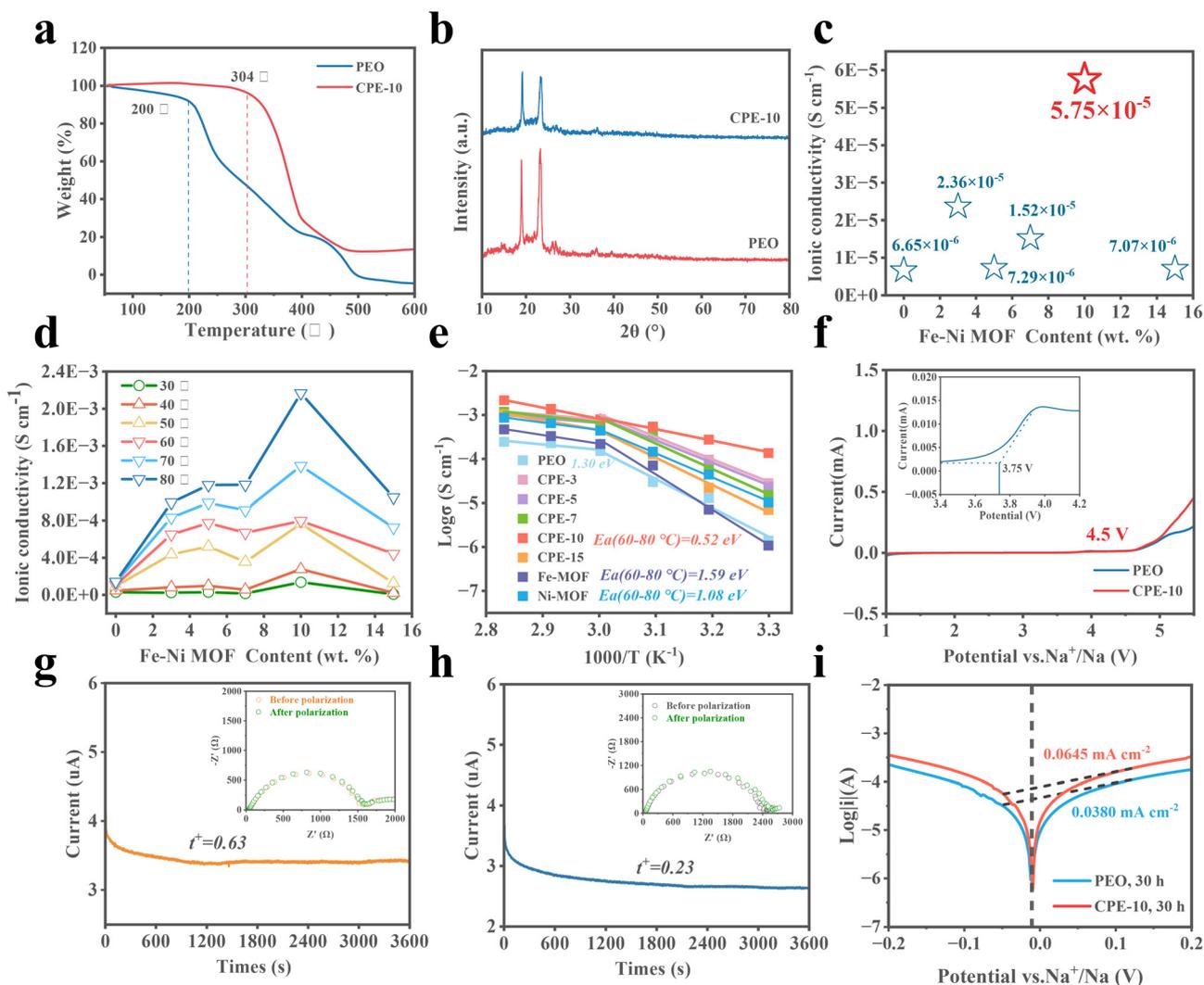
Fig. 3 (a) TGA curves and (b) XRD patterns of PEO and CPE-10. (c) Ionic conductivity of CPEs with different mass fractions of the Fe−Ni MOF at room temperature. (d) Ionic conductivity of CPEs with varying contents of Fe−Ni MOF. (e) Arrhenius plots of the ionic conductivity of CPEs. (f) LSV curves of PEO and CPE-10. (g and h) AC polarization curves of Na//Na cells using CPE-10 and PEO, with EIS curves (inset) before and after polarization. (i) Tafel plot comparison of Na//Na cells based on CPE-10 and PEO after 30 h of cycling.

and Ni-MOF CPE. Fig. 3d shows the ionic conductivity for different Fe−Ni MOF contents (0–15 wt%) of CPE-X (X = 0, 3, 5, 7, 10, 15) at different temperatures. With an increase in Fe−Ni MOF content, the ionic conductivity of CPEs initially increased and then decreased, reaching a maximum at 10 wt%. Specifically, the ionic conductivity of CPE-10 reaches 1.37×10^{-4} S cm^{-1} at 30 °C and 7.96×10^{-4} S cm^{-1} at 60 °C, which are much higher than those of PEO, Fe-MOF CPE and Ni-MOF CPE (Table S2). The Arrhenius plots of CPEs with different Fe−Ni MOF contents and the CPEs with single metal MOFs are shown in Fig. 3e. When the content of the Fe−Ni MOF was insufficient or excessive in CPE-X (X = 0, 3, 5, 7, 15), Fe-MOF CPE and Ni-MOF CPE, the Arrhenius plots show a turning point around 50 °C. This indicates higher activation energy below the turning point (greater than 1.0 eV) and lower Na$^+$ conductivity within the temperature range of 30–50 °C. When the temperature exceeded the polymer melting point (48 °C),

the activation energy became very small (approximately 0.3–0.4 eV), activating the diffusion behavior of Na$^+$. The Arrhenius plot of the optimized CPE-10 showed a nearly linear relationship across the entire temperature range with an activation energy of 0.50 eV. Therefore, the high ionic conductivity behavior can be extended to lower temperature regions. The increase in ionic conductivity is attributed to the transfer of Na$^+$ between the amorphous PEO domain and the Fe−Ni MOF interface ensuring uninterrupted high-speed migration of Na$^+$. Furthermore, linear sweep voltammetry (LSV) was adopted to evaluate the electrochemical stability of CPE-10 and PEO electrolytes (Fig. 3f). The results indicate that CPE-10 exhibits higher electrochemical stability within the voltage range of 1–4.5 V with no detectable decomposition current below 4.5 V (*vs.* Na$^+$/Na), indicating excellent antioxidative properties,[36] while the PEO electrolyte showed a decomposition current at 3.75 V, indicating poorer antioxidative properties.[37] Besides,

the migration of anions during cycling can lead to severe concentration polarization, causing sodium dendrite growth and interface side reactions, hindering the normal operation of the cell at high current densities. Therefore, electrolytes with a high Na^+ transference number are ideal for reducing concentration polarization and suppressing side reactions, thereby contributing to excellent energy storage performance. The Na^+ transference number of CPE-10 is 0.63, nearly three times that of PEO (0.23) (Fig. 3g and h),[38] which is significantly higher than that of the single metal Fe-MOF ($t^+ = 0.47$) and Ni-MOF ($t^+ = 0.48$) (Fig. S9, S10 and Table S3). It highlights the recognition function of the bimetallic MOF as the host molecule for the guest molecule $TFSI^-$. The bimetallic MOF can effectively recognize and confine the anions, thereby increasing the mobility of the cations. Fig. 3i presents a comparison of Tafel plots, showing enhanced Na^+ transport kinetics at the Na/polymer interface in CPE-10 after 30 h of cycling, as evidenced by a significant increase in the exchange current density (6.45×10^{-2} mA cm^{-2}). In contrast, the exchange current density of PEO is 3.80×10^{-2} mA cm^{-2}, nearly double that of CPE-10. However, at 0 h of cycling, the initial exchange current density of PEO is an order of magnitude higher than that of CPE-10, and the exchange current density of CPE-10 remains almost unchanged before and after cycling, indicating a more stable interface (Fig. S11). This demonstrates that symmetric cells using CPE-10 exhibit faster mass transfer kinetics at the Na/polymer interface.

In situ Raman characterization of host–guest interaction and ionic transport mechanisms in CPE-10

In situ Raman spectra reveal that the peak intensity of $TFSI^-$ (739 cm^{-1}) in PEO initially increases and then decreases during the charging process, with only a very small amount of sodium salt dissociating in the initial charging phase, indicating a higher degree of anion mobility within the system. In contrast, the peak intensity remains relatively stable in CPE-10 (Fig. 4a and b). This stability suggests that the bimetallic MOF in CPE-10 acts as a host to recognize the salts within the system, thereby restraining the anions. Besides, *ex situ* Raman spectra measurements were performed on CPE-10 and PEO (Fig. S12). There are two main states of $TFSI^-$ anions in the PEO-based electrolyte, namely dissociated (uncoordinated) $TFSI^-$ and ion clusters (two $TFSI^-$ ions coordinated with Na^+).[39] The percentage of free $TFSI^-$ in PEO is 66.8%, whereas in CPE-10, it reaches 87.7%. This proves that the Fe–Ni MOF as a Lewis-acid induces better decomposition of Na-$[TFSI]_n$ ion clusters. Fourier transform infrared (FTIR) spectra of the Fe–Ni MOF, PEO, and CPE-10 are shown in Fig. 4c. The introduction of the Fe–Ni MOF filler also affects the vibration of CH_2, resulting in weakening of peaks corresponding to symmetric stretching and bending vibrations of CH_2 at 2881 cm^{-1} and 1463 cm^{-1}, respectively.[40] The vibration at 1340 cm^{-1} of CH_2 weakens due to the strong vibration of the C–O–C group and its chain effect.[41] The abnormal decrease in vibration intensity at 1096 cm^{-1} (related to symmetric stretching of C–O–C) is likely due to the strong interference from the Lewis-acid

centers of the Fe–Ni MOF.[42] The peak at 842 cm^{-1} corresponds to the stretching vibration of CH_2CH_2O. FTIR results indicate that the strong interactions between the Fe–Ni MOF and PEO chains promote the vibration of C–O–C groups, facilitating the establishment of highly conductive interfaces between polymer chains and fillers.[43] This enhanced interaction improves Na^+ transport across the polymer–filler interface, contributing to higher ionic conductivity and better electrochemical performance of the electrolyte. Furthermore, molecular dynamics simulations (MDs) were used to assess the diffusion dynamics of Na^+ in the two electrolytes, as shown in Fig. 4d and S13. In the PEO electrolyte, the simulation results indicate that the polymer chains are randomly dispersed, and the transport of Na^+ follows a hopping mechanism within these chains. Na^+ moves from one coordination site to another, facilitated by the motion of polymer chain segments, leading to a random and anisotropic migration process for Na^+ in PEO, posing challenges for achieving rapid Na^+ migration. In contrast, in the CPE-10 electrolyte, the MDs results show that the introduction of the Fe–Ni MOF promotes the directional and orderly migration of Na^+.[44] From the coordination number ($n(r)$, dashed line) and radial distribution function ($g(r)$, solid line) shown in Fig. 4e, for the PEO system, the interaction probability of $O_{TFSI}\cdots Na$ at 2.3 Å and 4.5 Å indicates higher interactions between Na^+ and $TFSI^-$ suggesting a lower concentration of free Na^+ in the system. However, in CPE-10, the coordination effect of $O_{TFSI}\cdots Na$ is weaker compared to that of PEO, so the addition of the Fe–Ni MOF promotes the dissociation of NaTFSI, consistent with the Raman spectroscopy results. Additionally, the mean square displacement (MSD) analysis qualitatively assesses the diffusion rate of Na^+ in solid electrolyte systems. Fig. 4f shows the MSD curves for CPE-10 and PEO. The results indicate that CPE-10 significantly enhances the diffusion rate of Na^+, reaching up to 2.12×10^{-6} cm^2 S^{-1}, an order of magnitude higher than that of PEO (4.9×10^{-7} cm^2 S^{-1}), demonstrating the outstanding ability of CPE-10 to facilitate rapid Na^+ transport. To substantiate the host role of the Fe–Ni bimetallic MOF, we conducted theoretical calculations to explore the microscopic interactions between NaTFSI and the Fe–Ni MOF (Fig. 4g). The Fe–Ni MOF leads to lower binding energy between Na^+ and $TFSI^-$, indicating a higher dissociation degree of NaTFSI and enhanced Na^+ mobility. Moreover, the Fe–Ni MOF exhibits a higher adsorption energy for $TFSI^-$, enabling effective recognition of $TFSI^-$. Meanwhile, the binding energy between $TFSI^-$ and the Fe-MOF is −0.27 eV, and the binding energy between $TFSI^-$ and the Ni-MOF is −0.55 eV (Fig. S14), both of which are significantly weaker than that of the Fe–Ni bimetallic MOF, aligning with its lower Na^+ transference number. Additionally, electrostatic potential results indicate that introduction of the Fe–Ni bimetallic MOF into the PEO system weakens the binding energy between EO bonds and Na^+, while enhancing the binding energy between $TFSI^-$ and the Fe–Ni bimetallic MOF, achieving a unique "killing two birds with one stone" effect (Fig. S15). The mechanism of fast sodium ion transport was revealed by calculating the migration energy barriers (Fig. 4h).
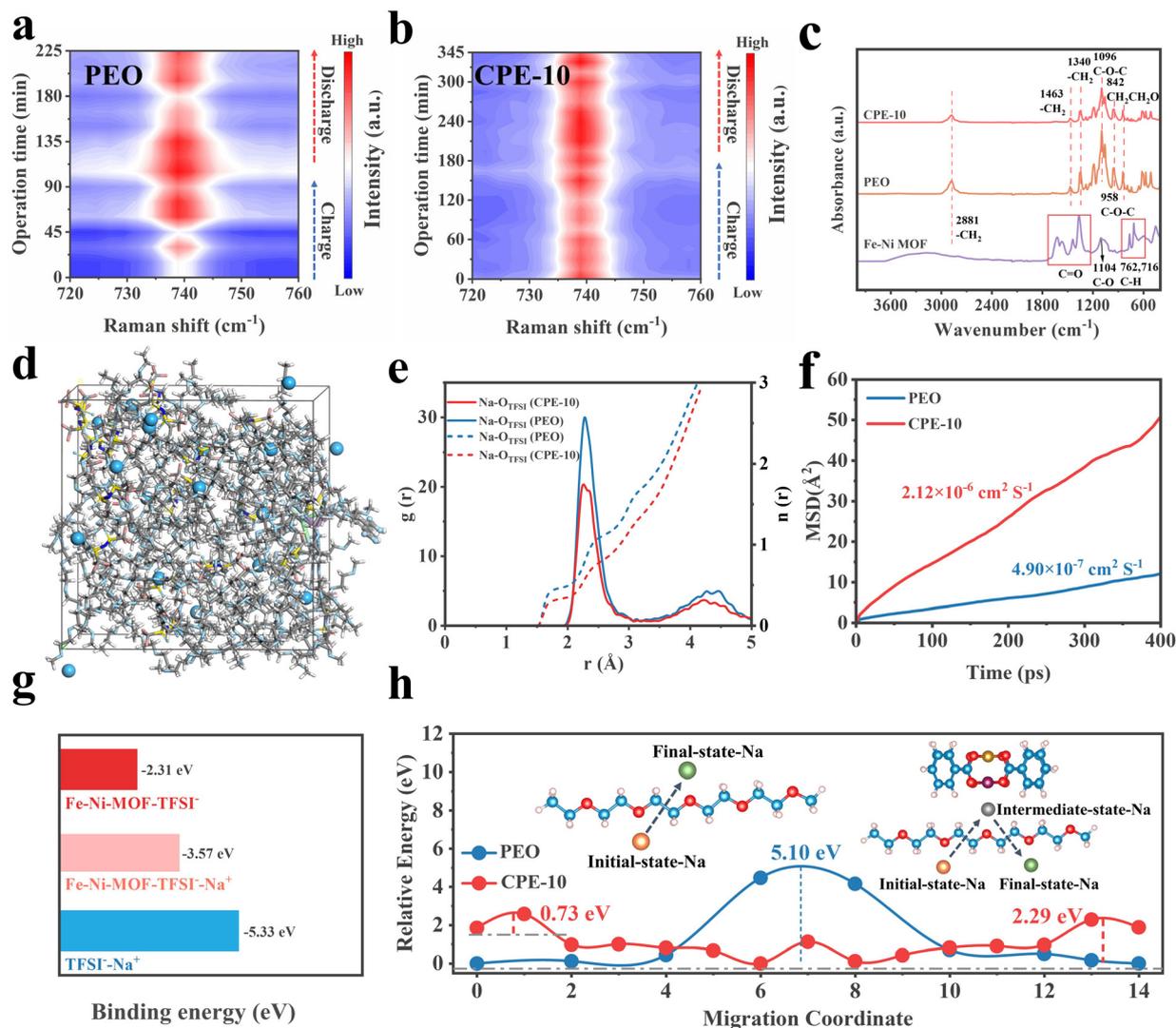
Fig. 4 (a and b) *In situ* Raman spectra under full cell operation. (c) FTIR spectra of the Fe–Ni MOF, PEO and CPE-10. (d) Snapshot of CPE-10/NaTFSI obtained by MDs. (e) Calculated radial distribution functions ($g(r)$, solid lines) and coordination numbers ($n(r)$, dashed lines) for Na–O_{TFSI} in different environments. (f) MSD of Na$^+$ in PEO and CPE-10 calculated from MDs. Here, the slope values are the linear fitting results for MSD. (g) The binding ability comparison of Fe–Ni MOF-TFSI$^-$, Fe–Ni-MOF-TFSI$^-$-Na$^+$ and Na$^+$-TFSI$^-$ in CPE-10. (h) Migration energy barriers of Na$^+$ diffusion pathways in PEO and CPE-10 electrolytes. Inset: (left) Na$^+$ migration pathway within PEO chains in the PEO system; (right) Na$^+$ migration pathway within PEO chains in the CPE-10 system.

In PEO, the energy barrier for Na$^+$ migration from the initial Na site to the final Na site is relatively high, at 5.10 eV. Conversely, in CPE-10, the migration energy barrier from the asymmetric initial Na site to the intermediate Na site is 0.73 eV, while the barrier from the intermediate Na site to the final Na site is only 2.29 eV. This indicates that in the Fe–Ni MOF-modified electrolyte, Na$^+$ is more likely to undergo rapid migration along the disentangled PEO chain segments.

Na metal compatibility and interfacial analysis of Na metal

To examine the electrochemical stability of CPE-10 with the sodium anode, a galvanostatic charge–discharge cycling test was conducted on Na/Na symmetrical cells. Fig. 5a demon-strates the periodic charge–discharge curves at 0.05 mA cm^{-2} and 25 °C, where the symmetrical cells assembled with CPE-10 exhibited a relatively flat polarization curve and were able to cycle stably for over 1150 h. In contrast, the cell assembled with PEO short-circuited in less than 5 h, revealing superior interfacial stability of CPE-10 with the Na anode. Meanwhile, the symmetric cells assembled with CPE-10 can also cycle stably for 1200 h at 60 °C and a current density of 0.1 mA cm^{-2} (Fig. S16). Furthermore, rate cycling at different current densities also showed that CPE-10 has a better ability to resist dendrite formation compared to PEO (Fig. S17). Fig. 5b and c show the SEM images of Na/CPE-10/Na and Na/PEO/Na symmetrical cells after 50 h of cycling. The sodium surface of the
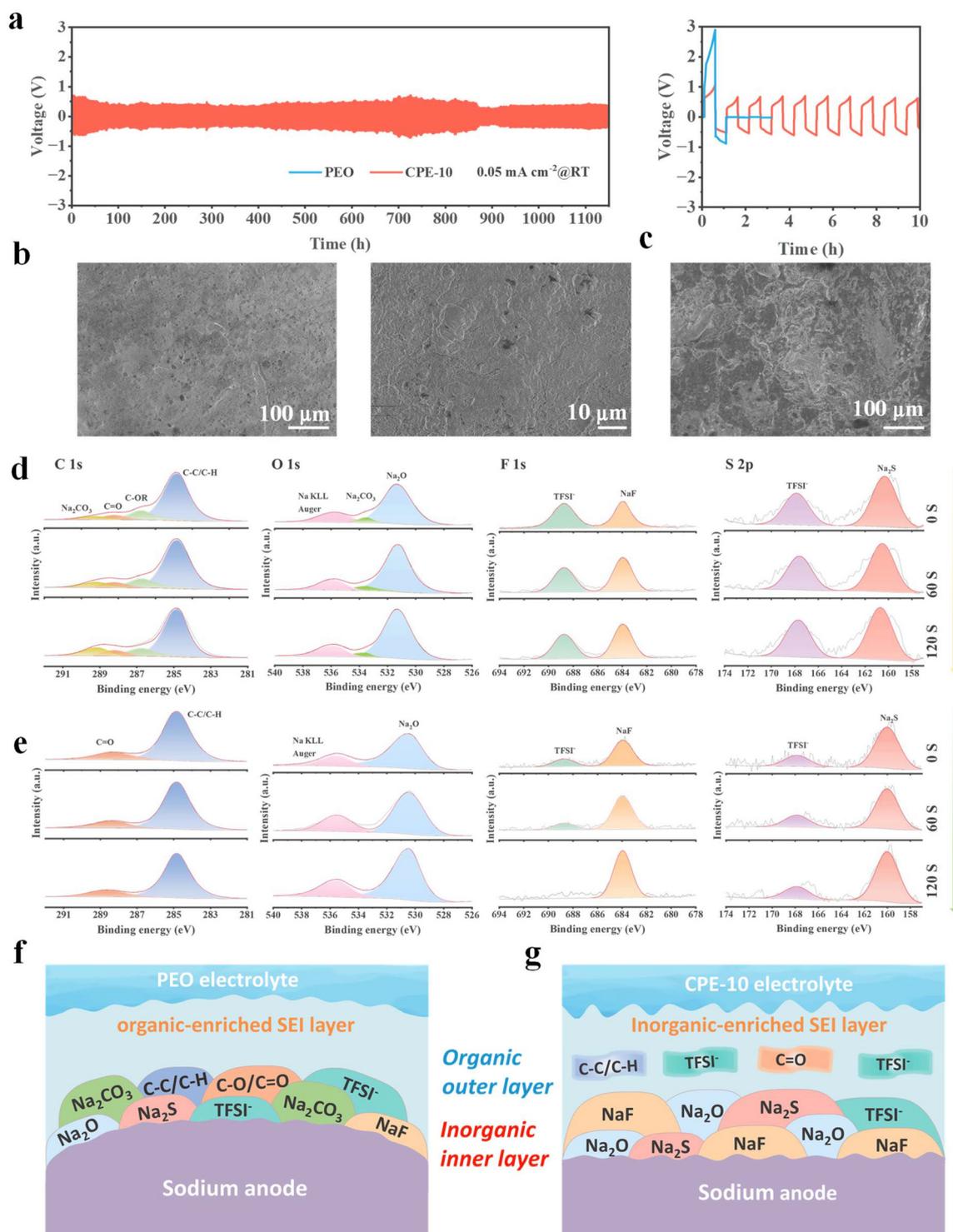
Fig. 5 (a) Comparison of cycling performance of Na/Na symmetric cells with the CPE-10 and PEO electrolytes plating/stripping at 0.05 mA cm^{-2} for 30 min. The inset shows the enlarged view of cycle stages at 25 °C. The SEM images of the Na anode after cycling for 50 h for (b) Na/CPE-10/Na and (c) Na/PEO/Na cells. *Ex situ* XPS measurements of the sodium metal anode surface, etched for 60 s and 120 s after cycling for 50 h for (d) PEO and (e) CPE-10 systems, with the signals of C 1s, O 1s, F 1s and S 2p. Schematic illustration of components at the surface of the cycled sodium metal anode based on (f) PEO and (g) CPE-10.

PEO-based cell exhibited dendrites, an uneven surface, and signs of instability. On the other hand, the sodium surface of the Na/CPE-10/Na cell remained smooth and flat at both large and small scales, confirming uniform sodium deposition and thus greater stability of the sodium anode. To analyze the composition of the sodium surface after cycling, *ex situ* XPS measurements were performed on the sodium anode, as shown in Fig. 5d and e. The C 1s spectrum of the PEO system consists of a C–C/C–H peak at 284.8 eV, C–O peak at 286.7 eV, C=O peak at 288.2 eV, and Na_2CO_3 peak at 289.3 eV, and as the etching time increased from 60 s to 120 s, the Na_2CO_3 peak gradually intensified.[45] However, in the CPE-10 system, the Na_2CO_3 peak did not appear, and the C–O peak increased. With the introduction of the Fe–Ni MOF as a Na^+ modulator, the Na_2CO_3 signal was absent in the O 1s spectrum, while the Na_2O peak at 531.4 eV gradually intensified with etching time.[46] The F 1s spectrum also showed that in the CPE-10 system, the NaF peak at 684.0 eV gradually intensified, and the $TFSI^-$ peak at 688.8 eV gradually attenuated, almost completely disappearing after etching for 120 s.[47] Conversely, in the PEO system, the NaF peak was relatively weak, and there was a significant presence of $TFSI^-$. The S 2p spectra showed similar results, with the Na_2S peak at 159.9 eV in the PEO system gradually decreasing as the etching depth increased.[48] The results indicate that the residual Na_2CO_3, captured $TFSI^-$, and its decomposition products passivated the interface of the PEO system, resulting in poor cycling performance (Fig. 5f). However, the Fe–Ni MOF as a Na^+ modulator could better adsorb $TFSI^-$, allowing it to diffuse to the sodium anode. Therefore, the O atoms at the end of the PEO segment near the sodium metal tend to become sodiated, forming Na_2O and retaining the C–O groups. The capture and degradation of $TFSI^-$ on the sodium anode were mitigated and no additional carbon source was provided for the conversion of Na_2O to Na_2CO_3. Meanwhile, it has been found that Na_2O and NaF exhibit excellent affinity for sodium ions. Their abundant presence in the SEI layer promotes the formation of smooth, non-dendritic sodium deposition, whereas a deficiency or insufficient content leads to rough, moss-like accumulation on the sodium surface, facilitating dendrite growth. Moreover, NaF is more effective than Na_2O in suppressing vertical dendrite formation, and its high interfacial energy promotes lateral migration of sodium along the interface, enhancing the SEI's dendrite-suppressing capability. Sodium ions also migrate more easily in Na_2O and NaF; while migration in Na_2CO_3 is hindered and electronically insulating, excessive Na_2CO_3 can cause SEI instability and increased cell impedance.[6,46,49] Taken together, constructing an organic–inorganic gradient SEI rich in Na_2O, NaF, and Na_2S with a small amount of Na_2CO_3 can simultaneously facilitate sodium ion transport and improve long-term cycling stability (Fig. 5g).

Electrochemical performance and compatibility of CPE-10 with various cathodes

The full-cells were assembled using $Na_3V_2(PO_4)_3$ (NVP) as the cathode and sodium as the anode to further evaluate the cell performance. As shown in Fig. 6a, the all-solid-state NVP/CPE-10/Na cell exhibits an initial discharge capacity of 91.37 mAh g^{-1} at 0.2C and 25 °C. After 350 cycles, the capacity retention rate is as high as 95.06%, with minimal polarization observed in the later cycles (Fig. 6b). In contrast, the full battery based on PEO cannot cycle normally at room temperature due to its low ionic conductivity. Fig. 6c shows the comparison of the rate performance of NVP/CPE-10/Na and NVP/PEO/Na cells. Compared to the NVP/PEO/Na cell, the NVP/CPE-10/Na cell exhibits superior rate performance. At 60 °C, the discharge capacities at current densities of 0.3C, 0.5C, 1C, 1.5C, and 2C are 90.4 mAh g^{-1}, 90.3 mAh g^{-1}, 88.2 mAh g^{-1}, 87.4 mAh g^{-1}, and 85.6 mAh g^{-1}, respectively (Fig. S18). Notably, the capacity can recover to its initial value when the current density returns to 0.3C, indicating high electrochemical reversibility of the NVP/CPE-10/Na cell. During cycling at 0.2C and 60 °C (Fig. S19), the initial discharge specific capacity of the NVP/CPE-10/Na cell is 80.6 mAh g^{-1}, with a lower capacity at the early stage. However, as cycling progresses, the discharge specific capacity gradually increases and reaches a stable value of 112.8 mAh g^{-1} due to interface activation and stabilization. After 210 cycles, the discharge specific capacity is still 111.4 mAh g^{-1}, with a capacity retention rate of 98.8%. This performance is significantly better than that of the NVP/PEO/Na cell, which exhibits a lower discharge specific capacity at 0.2C and experiences overcharging after 123 cycles, resulting in battery failure (Fig. S20). The rate performance of the full-cells based on CPE-10 at 0.2C surpasses any relevant electrolyte level reported to date (Fig. 6e and Table S4). When the current density is increased to 1C (Fig. 6d), the initial discharge specific capacity is 100.6 mAh g^{-1} for the NVP/CPE-10/Na cell, and after 600 cycles, the capacity retention rate is still as high as 97.2%. SMBs assembled with the Fe-MOF CPE and Ni-MOF CPE as electrolytes can both cycle normally at 1C, but their discharge specific capacities are relatively low, and they exhibit significant polarization during cycling (Fig. S21). The NVP/Fe-MOF CPE/Na cell shows overcharging after 107 cycles, while the NVP/Ni-MOF CPE/Na cell can cycle normally for 300 cycles, but its interface is highly unstable, with fluctuating curves, and the capacity after 300 cycles is only 15.9 mAh g^{-1}. Therefore, SMBs assembled with CPEs based on single-metal MOFs exhibit poor performance, mainly because single metals are less stable during cycling compared to bimetals, and their lower ion transport capacity leads to severe concentration polarization, resulting in unstable interfaces. The cycling impedance test at 1C revealed that the interface impedance stabilized after 50 cycles (Fig. S22). When the current is increased to 2C, the cell can still operate stably for 3000 cycles, with an initial discharge specific capacity of 83.6 mAh g$^-$ (Fig. S23). After interface activation, its highest discharge specific capacity can reach 91.8 mAh g^{-1} with no significant polarization during cycling (Fig. S24). Additionally, the NVP/CPE-10/Na cell also exhibits good cycling performance at 45 °C (Fig. S25). These findings indicate that the prepared CPE-10 electrolyte is expected to be used at room to high temperatures, enabling
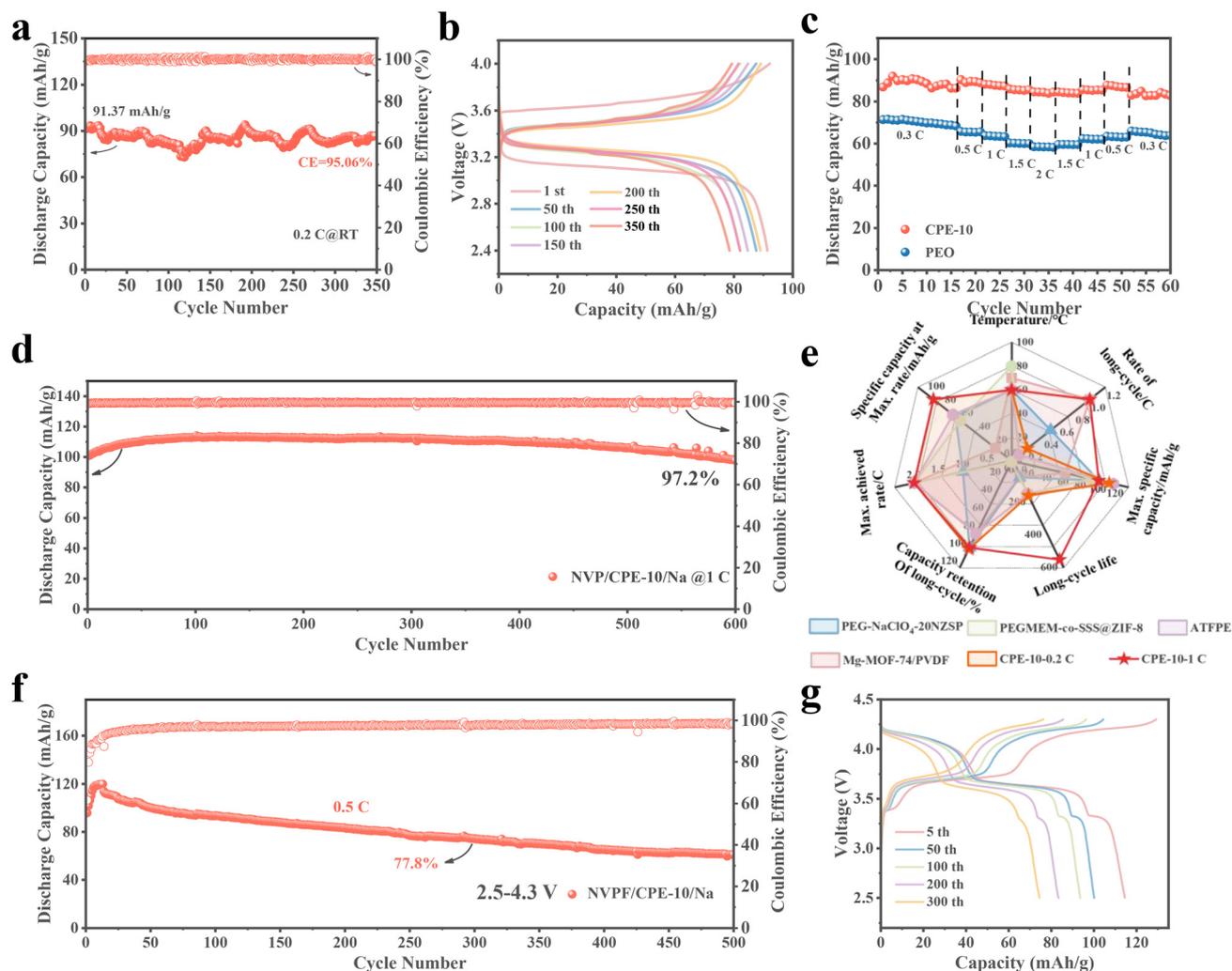
Fig. 6 (a and b) Cycling performance of the NVP/CPE-10/Na cell at 25 °C with a current density of 0.2C. (c) Rate performances (0.3–2C) of the NVP/PEO/Na and NVP/CPE-10/Na cells. (d) Cycling performance of the NVP/CPE-10/Na cells at 60 °C and 1C. (e) Comparison of CPE-based cells with the previously reported ASSMBs in terms of rate capability and long-term cycling performance. (f) Cycling performance of the NVPF/CPE-10/Na cells at 60 °C with a current density of 0.5C. (g) The corresponding voltage profile of the all-solid-state NVPF/CPE-10/Na at 0.5C in different cycles.

ASSMBs to be used over a wider temperature range. Given its electrochemical window reaching up to 4.5 V, a high-voltage sodium cell was assembled using $Na_3V_2(PO_4)_2F_3$ (NVPF) as the cathode and CPE-10 as the electrolyte. The long-term cycling performance at a rate of 0.5C was tested (Fig. 6f and g). The initial discharge specific capacity was 95.8 mAh g^{-1}, with the highest discharge specific capacity reaching 119.9 mAh g^{-1}. After 300 cycles, the capacity retention rate was still 77.8%. No short-circuit or overcharging occurred during the cell cycling process. The all-solid-state NVPF-based sodium cell assembled with CPE-10 as the electrolyte exhibited excellent electrochemical performance, laying a foundation for subsequent high-voltage sodium batteries.

Considering potential practical applications, solid-state sodium metal pouch cells were assembled using CPE-10 as the electrolyte and tested under various mechanical abuses

(Fig. 7d). Their overall superior performance enabled the fabrication of a foldable all-solid-state pouch cell. The cell could continuously light a bulb when folded and even when the entire cell was repeatedly folded. Besides, the all-solid-state pouch cell with a cathode loading of 2.1 mg cm^{-2} could stably cycle for 56 cycles at 0.1C (Fig. 7a), with an initial discharge specific capacity of 113.4 mAh g^{-1}. The charge–discharge curves of the first three cycles exhibit a high degree of overlap (Fig. 7b). Even the pouch cell assembled with a higher cathode loading of 4.0 mg cm^{-2} could steadily cycle for 30 cycles at 0.1C, with a capacity retention of up to 97.8% (Fig. 7c).

In conclusion, the proposed CPE-10 in ASSMBs exhibits high safety and excellent electrochemical performance, demonstrating promising application potential in future high-energy-density storage systems.
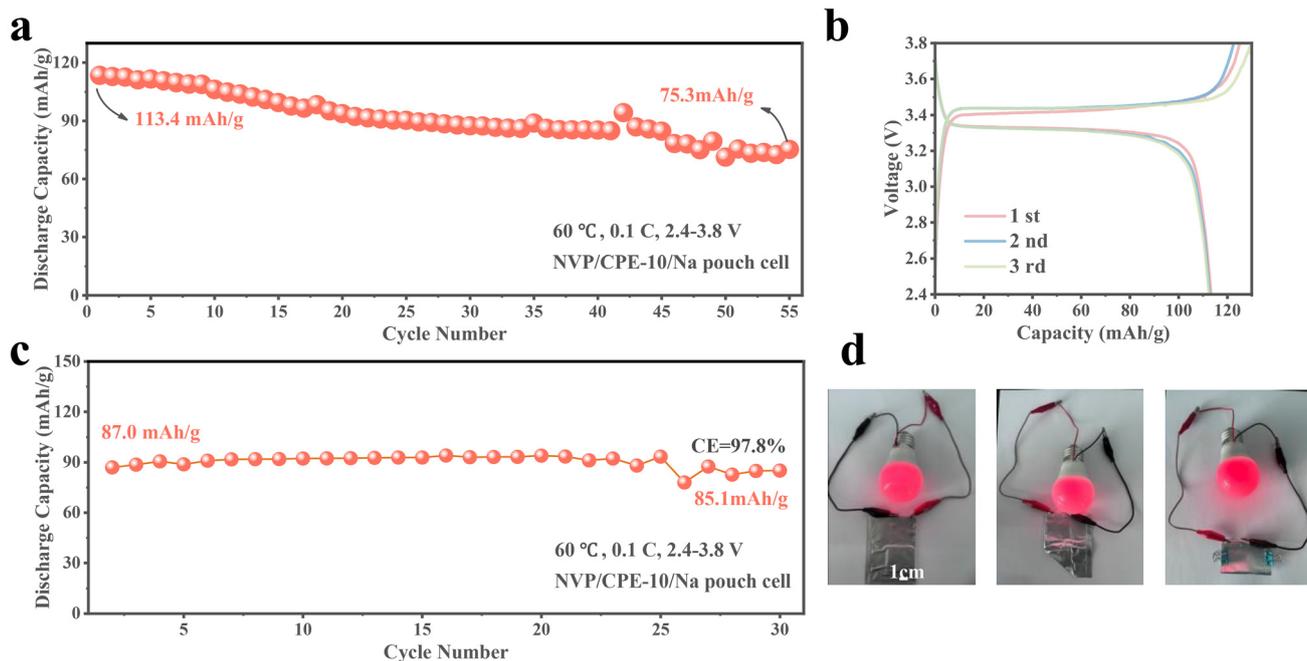
Fig. 7 (a) Cycling performance of the pouch-type all-solid-state NVP/CPE-10/Na cell at 0.1C with a cathode loading of 2.1 mg cm^{-2}. (b) Corresponding charge–discharge curves of the pouch-type NVP/CPE-10/Na cell at different cycling stages. (c) Cycling performance of the pouch-type all-solid-state NVP/CPE-10/Na cell at 0.1C with a cathode loading of 4.0 mg cm^{-2}. (d) Lighting test of the NVP/CPE-10/Na pouch cell under repeated bending and folding.

Conclusions

In summary, we demonstrated ultra-stable ASSMBs using a composite polymer electrolyte enhanced using a bimetallic MOF structure that selectively promotes rapid Na$^+$ transport. Our results confirm that the bimetallic MOF reduces the Na$^+$ diffusion energy barrier by decreasing the polymer crystallinity and providing continuous Na$^+$ transport pathways. *In situ* Raman spectroscopy and molecular dynamics simulations further confirm the strong Lewis acid–base interactions between the bimetallic MOF and TFSI$^-$, thereby enhancing the Na$^+$ migration capability. Consequently, the Na$^+$ transference number significantly increases (from 0.23 to 0.63), enabling the symmetric cell to operate stably for 1150 h. Based on the bimetallic MOF-enhanced PEO-based polymer electrolyte, the ASSMBs combined with an NVP cathode exhibit significantly enhanced cycling stability, excellent rate capability, and outstanding wide-temperature performance. The pouch cell remains functional and continues to power a bulb under mechanical abuse, and its capacity stays stable over long cycles even with a high cathode loading of 4.0 mg cm^{-2}, demonstrating the potential of CPE-10 for practical applications. This work provides meaningful insights into the design of high-performance polymer electrolytes for practically feasible all-solid-state sodium metal batteries.

Conflicts of interest

The authors declare no conflict of interest.

Data availability

All data generated or analyzed during this study are included in this manuscript and its SI. Supplementary information incorporates the experimental data, XPS spectra, element analysis, BET test, and electrochemical performance of different samples. Supplementary information is available. See DOI: https://doi.org/10.1039/d5eb00117j.

Acknowledgements

References

1 X. E. Wang, C. Zhang, M. Sawczyk, Q. H. Yuan, F. F. Chen, T. C. Mendes, P. C. Howlett, C. K. Fu, P. Kral, C. J. Hawker, A. Whittaker, M. Forsyth, J. Sun, Y. Q. Wang, X. Tan and D. J. Searles, *Nat. Mater.*, 2022, **21**, 1057–1065.

2 Z. P. Li, K. J. Zhu, P. Liu and L. F. Jiao, *Adv. Energy Mater.*, 2022, **12**, 100359.

3 J. H. Guo, F. Feng, S. Q. Zhao, Z. H. Shi, R. Wang, M. Yang, F. F. Chen, S. L. Chen, Z. F. Ma and T. X. Liu, *Carbon Energy*, 2023, **5**, e314.

4 P. Jaumaux, J. R. Wu, D. Shanmukaraj, Y. Z. Wang, D. Zhou, B. Sun, F. Y. Kang, B. H. Li, M. Armand and G. X. Wang, *Adv. Funct. Mater.*, 2021, **31**, 2008644.

5 P. Lennartz, B. A. Paren, A. Herzog-Arbeitman, X. C. Chen, J. A. Johnson, M. Winter, Y. Shao-Horn and G. Brunklaus, *Joule*, 2023, **7**, 1471–1495.

6 X. R. Dong, Y. Zhang, Z. C. You, Y. M. Chen, X. W. Wu and Z. Y. Wen, *Adv. Funct. Mater.*, 2024, **34**, 2405931.

7 Y. Li, F. Wu, Y. Li, M. Q. Liu, X. Feng, Y. Bai and C. Wu, *Chem. Soc. Rev.*, 2022, **51**, 4484–4536.

8 J. P. Hoffknecht, A. Wettstein, J. Atik, C. Krause, J. Thienenkamp, G. Brunklaus, M. Winter, D. Diddens, A. Heuer and E. Paillard, *Adv. Energy Mater.*, 2023, **13**, 202789.

9 N. Meng, Y. N. Ye, Z. X. Yang, H. Li and F. Lian, *Adv. Funct. Mater.*, 2023, **33**, 2305072.

10 H. Li, Y. F. Du, Q. Zhang, Y. Zhao and F. Lian, *Adv. Energy Mater.*, 2022, **12**, 2103530.

11 Y. Wei, H. J. Zhou, H. Deng, W. J. Ji, K. Tian, Z. Y. Ma, K. Y. Zhang and Q. Fu, *Nano-Micro Lett.*, 2022, **14**, 35.

12 S. Li, S. Q. Zhang, L. Shen, Q. Liu, J. B. Ma, W. Lv, Y. B. He and Q. H. Yang, *Adv. Sci.*, 2020, **7**, 1903088.

13 Z. B. Liang, C. Qu, W. H. Guo, R. Q. Zou and Q. Xu, *Adv. Mater.*, 2018, **30**, 1702891.

14 Z. W. Cao, R. Momen, S. S. Tao, D. Y. Xiong, Z. R. Song, X. H. Xiao, W. T. Deng, H. S. Hou, S. Yasar, S. Altin, F. Bulut, G. Q. Zou and X. B. Ji, *Nano-Micro Lett.*, 2022, **14**, 181.

15 L. Q. Xu, X. H. Xiao, H. Y. Tu, F. J. Zhu, J. Wang, H. X. Liu, W. Y. Huang, W. T. Deng, H. Hou, T. C. Liu, X. B. Ji, K. Amine and G. Q. Zou, *Adv. Mater.*, 2023, **35**, 2303193.

16 T. Kim, S. Hyeok Ahn, Y. Y. Song, B. Jin Park, C. Lee, A. Choi, M. H. Kim, D. H. Seo, S. K. Jung and H. W. Lee, *Angew. Chem., Int. Ed.*, 2023, **62**, e202309852.

17 T. W. Kim, K. H. Park, Y. E. Choi, J. Y. Lee and Y. S. Jung, *J. Mater. Chem. A*, 2018, **6**, 840–844.

18 J. Park, D. Han, J. P. Son, H. Kwak, W. Ko, C. Park, C. Lee, H.-W. Lee, J. Kim, K.-W. Nam and Y. S. Jung, *ACS Energy Lett.*, 2024, **9**, 2222–2230.

19 T.-U. Wi, S. O. Park, S. J. Yeom, M.-H. Kim, I. Kristanto, H. Wang, S. K. Kwak and H.-W. Lee, *ACS Energy Lett.*, 2023, **8**, 2193–2200.

20 A. M. Mohamed, M. Ramadan and N. K. Allam, *J. Energy Storage*, 2021, **34**, 102195.

21 Z. W. Lei, J. L. Shen, W. D. Zhang, Q. R. Wang, J. Wang, Y. H. Deng and C. Y. Wang, *Nano Res.*, 2020, **13**, 2259–2267.

22 J. F. Zhang, Y. Y. Wang, Q. B. Xia, X. F. Li, B. Liu, T. P. Hu, M. Tebyetekerwa, S. L. Hu, R. Knibbe and S. L. Chou, *Angew. Chem., Int. Ed.*, 2024, **63**, e202318822.

23 L. Zhao, J. Yan, H. Huang, X. Du, H. Chen, X. He, W. Li, W. Fang, D. Wang, X. Zeng, J. Dong and Y. Liu, *Adv. Funct. Mater.*, 2023, **34**, 2310902.

24 X. Liu, R. Liu, J. Qiu, X. Cheng and G. Li, *Angew. Chem., Int. Ed.*, 2020, **59**, 13962–13967.

25 L. Xu, X. Xiao, H. Tu, F. Zhu, J. Wang, H. Liu, W. Huang, W. Deng, H. Hou, T. Liu, X. Ji, K. Amine and G. Zou, *Adv. Mater.*, 2023, **35**, 2303193.

26 J. H. Guo, F. Feng, X. Y. Jiang, R. Wang, D. K. Chu, Y. F. Ren, F. F. Chen, P. He, Z. F. Ma, S. L. Chen and T. X. Liu, *Adv. Funct. Mater.*, 2024, **34**, 2313496.

27 Y. F. Li, W. J. Ma, H. H. Yang, Q. Y. Tian, Q. Xu and B. X. Han, *Chem. Commun.*, 2022, **58**, 6833–6836.

28 J. L. Hu, C. Z. Lai, K. Y. Chen, Q. P. Wu, Y. P. Gu, C. L. Wu and C. L. Li, *Nat. Commun.*, 2022, **13**, 7914.

29 F. F. Zheng, C. W. Li, Z. C. Li, X. Cao, H. B. Luo, J. Liang, X. D. Zhao and J. Kong, *Small*, 2023, **19**, 2206355.

30 X. W. Yu, Y. J. Liu, J. B. Goodenough and A. Manthiram, *ACS Appl. Mater. Interfaces*, 2021, **13**, 30703–30711.

31 G. Xi, M. Xiao, S. J. Wang, D. M. Han, Y. N. Li and Y. Z. Meng, *Adv. Funct. Mater.*, 2021, **31**, 2007598.

32 Y. Q. Liao, L. X. Yuan, Y. Han, C. F. Liang, Z. Z. Li, Z. Li, W. Luo, D. H. Wang and Y. H. Huang, *Adv. Mater.*, 2024, **36**, 2312287.

33 X. Q. Huang, Z. P. Zhao, L. Cao, Y. Chen, E. B. Zhu, Z. Y. Lin, M. F. Li, A. M. Yan, A. Zettl, Y. M. Wang, X. F. Duan, T. Mueller and Y. Huang, *Science*, 2015, **348**, 1230–1234.

34 Y. Yang, Z. Y. Lin, S. Q. Gao, J. W. Su, Z. Y. Lun, G. L. Xia, J. T. Chen, R. R. Zhang and Q. W. Chen, *ACS Catal.*, 2017, **7**, 469–479.

35 G. Liu, M. Reinhout, B. Mainguy and G. L. Baker, *Macromolecules*, 2006, **39**, 4726–4734.

36 J. Y. Zhang, Y. L. Yan, X. Wang, Y. Y. Cui, Z. F. Zhang, S. Wang, Z. K. Xie, P. F. Yan and W. H. Chen, *Nat. Commun.*, 2023, **14**, 3701.

37 S. D. Huo, L. Sheng, W. D. Xue, L. Wang, H. Xu, H. Zhang and X. M. He, *InfoMat*, 2023, **5**, e12394.

38 H. Zhang, C. M. Li, M. Piszcz, E. Coya, T. Rojo, L. M. Rodriguez-Martinez, M. Armand and Z. B. Zhou, *Chem. Soc. Rev.*, 2017, **46**, 797–815.

39 N. Chen, Y. J. Dai, Y. Xing, L. L. Wang, C. Guo, R. J. Chen, S. J. Guo and F. Wu, *Energy Environ. Sci.*, 2017, **10**, 1660–1667.

40 R. Kumar, S. Sharma, D. Pathak, N. Dhiman and N. Arora, *Solid State Ionics*, 2017, **305**, 57–62.

41 X. Zhou, B. Zhang, F. Huang, F. Li, Z. Ma and J. Liu, *Nano Energy*, 2023, **108**, 108221.

42 T. Krahl, A. Vimont, G. Eltanany, M. Daturi and E. Kemnitz, *J. Phys. Chem. C*, 2007, **111**, 18317–18325.

43 S. J. Wen, T. J. Richardson, D. I. Ghantous, K. A. Striebel, P. N. Ross and E. J. Cairns, *J. Electroanal. Chem.*, 1996, **408**, 113–118.

44 J. Q. Sun, C. H. He, Y. G. Li, Q. H. Zhang, C. Y. Hou, M. De Volder, K. R. Li and H. Z. Wang, *Energy Storage Mater.*, 2023, **54**, 40–50.

45 S. Zhong, Y. S. Yu, Y. Yang, Y. Yao, L. F. Wang, S. N. He, Y. X. Yang, L. Liu, W. P. Sun, Y. Z. Feng, H. G. Pan, X. H. Rui and Y. Yu, *Angew. Chem., Int. Ed.*, 2023, **62**, e202301169.

46 M. Y. Xu, Y. Li, M. Ihsan-Ul-Haq, N. Mubarak, Z. J. Liu, J. X. Wu, Z. T. Luo and J. K. Kim, *Energy Storage Mater.*, 2022, **44**, 477–486.

47 J. Luo, M. R. Yang, D. H. Wang, J. Y. Zhang, K. M. Song, G. C. Tang, Z. K. Xie, X. N. Guo, Y. Shi and W. H. Chen, *Angew. Chem., Int. Ed.*, 2024, **62**, e202315076.

48 J. F. Liu, Z. Y. Wu, F. J. Stadler and Y. F. Huang, *Angew. Chem., Int. Ed.*, 2023, **62**, e202300243.

49 B. Qiu, N. Sun, X. Li, R. A. Soomro, Y. Guan, H. Mi and B. Xu, *Adv. Funct. Mater.*, 2025, e12543.